PROCESS DAMPING IDENTIFICATION FOR MULTIPLE DEGREE OF FREEDOM TURNING OPERATIONS

Christopher Tyler and Tony L. Schmitz
Mechanical Engineering and Engineering Science
University of North Carolina at Charlotte
Charlotte, NC, USA

INTRODUCTION

The analytical stability lobe diagram offers a predictive capability for selecting stable chip width-spindle speed combinations in machining operations. However, the increase in allowable chip width provided at spindle speeds near integer fractions of the system's dominant natural frequency is diminished substantially at low spindle speeds where the stability lobes are closely spaced. Fortunately, the process damping effect can serve to increase the chatter-free chip widths at these low speeds. This increased stability at low spindle speeds is particularly important for hard-to-machine materials that cannot take advantage of the higher speed stability zones due to prohibitive tool wear at high cutting speeds.

The objective of this study is expand on the work by Tyler and Schmitz [1] to identify and model process damping for multiple degree of freedom (MDOF) cutting systems. The level of process damping is measured for MDOF turning processes using flexure-based setups and compared to similar single degree of freedom (SDOF) results.

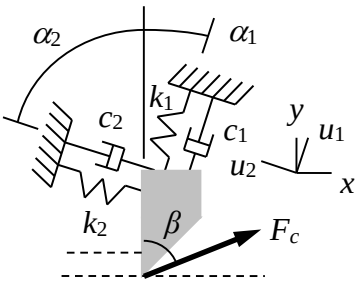

Figure 1: Turning model with a SDOF in two orthogonal directions.

MODEL

The turning model with a SDOF in two orthogonal directions is depicted in Fig. 1. The two mode directions, u_1 and u_2, are oriented at the angles α_1 and α_2, respectively, relative to the surface normal direction, y. The cutting force, F_c, is oriented at the force angle β. The variable component of the cutting force is described by Eq. 1, where K_s is the specific cutting force coefficient, b is the commanded chip width, Y_0 is the vibration amplitude in the y direction from the previous revolution, and Y is the current vibration amplitude. The difference between Y_0 and Y identifies the variable chip thickness due to the vibration from one revolution to the next and provides the basis for regenerative chatter. The mean component of the cutting force is excluded because it does not influence stability for the linear analysis presented here.

$$F_c = K_s b(Y_0 - Y) \tag{1}$$

The assumption for Eq. 1 is that there is no phase shift between the variable force and the chip thickness. This is indicated by the real values of b and K_s. However, it has been shown that a phase shift can occur at low cutting speeds. This phenomenon is captured by the inclusion of the process damping force, F_d, defined in Eq. 2 [2], where C is the process damping coefficient, V is the cutting speed, and $\dot{y}$ is the tool velocity in the y direction. The process damping force is oriented in the y direction and opposes the cutting force (as projected in the y direction). In other words, it is a viscous damping force. Therefore, the process damping force is used to modify the structural damping and obtain an analytical stability solution.

$$F_d = -C\frac{b}{V}\dot{y} \tag{2}$$

To proceed with the solution, the cutting and process damping forces are projected into the u_1 and u_2 directions as shown in Eqs. 3-4, where F_{c_1} and F_{c_2} are the cutting force components in the u_1 and u_2 directions.

$$F_{u_1} = F_c\cos(\beta - \alpha_1) - C\frac{b}{V}\dot{y}\cos(\alpha_1) = F_{c_1} - C\frac{b}{V}\dot{y}\cos(\alpha_1) \tag{3}$$

$$F_{u_2} = F_c \cos(\beta + \alpha_2) - C\frac{b}{V}\dot{y}\cos(\alpha_2) = F_{c_2} - C\frac{b}{V}\dot{y}\cos(\alpha_2) \quad (4)$$

The time domain equations of motion for the two directions are provided in Eqs. 5-6, where m_i, c_i, and k_i, i = 1, 2, are the mass, viscous damping coefficient, and stiffness for the single DOF structural dynamics. In these equations, one overdot indicates one time derivative (velocity) and two overdots indicate two time derivatives (acceleration).

$$m_1\ddot{u}_1 + c_1\dot{u}_1 + k_1u_1 = F_{c_1} - C\frac{b}{V}\dot{y}\cos(\alpha_1) \quad (5)$$

$$m_2\ddot{u}_2 + c_2\dot{u}_2 + k_2u_2 = F_{c_2} - C\frac{b}{V}\dot{y}\cos(\alpha_2) \quad (6)$$

The y direction velocity can be written as a function of the velocities in the u_1 and u_2 directions as shown in Eq. 7. Substitution of Eq. 7 into Eqs. 5-6 yields Eqs. 8-9. Even though the structural dynamics are uncoupled (orthogonal), the equations of motion for the two directions are now coupled through the $\dot{u}_1$ and $\dot{u}_2$ velocity terms.

$$\dot{y} = \dot{u}_1\cos(\alpha_1) + \dot{u}_2\cos(\alpha_2) \quad (7)$$

$$m_1\ddot{u}_1 + c_1\dot{u}_1 + k_1u_1 = F_{c_1} - C\frac{b}{V}(\dot{u}_1\cos(\alpha_1) + \dot{u}_2\cos(\alpha_2))\cos(\alpha_1) \quad (8)$$

$$m_2\ddot{u}_2 + c_2\dot{u}_2 + k_2u_2 = F_{c_2} - C\frac{b}{V}(\dot{u}_1\cos(\alpha_1) + \dot{u}_2\cos(\alpha_2))\cos(\alpha_2) \quad (9)$$

By assuming a solution of the form $u_1(t) = U_1e^{i\omega t}$ for harmonic motion, Eqs. 8-9 can be rewritten in the frequency domain (ω is frequency). The results are provided in Eqs. 10-11, where the U_1 and U_2 terms have been grouped on the left hand side in both equations and the $e^{i\omega t}$ term has been dropped from both sides in each case.

$$\left(-m_1\omega^2 + i\omega\left(c_1 + C\frac{b}{V}(\cos(\alpha_1))^2\right) + k_1\right)U_1 + i\omega\left(C\frac{b}{V}\cos(\alpha_1)\cos(\alpha_2)\right)U_2 = F_{c_1} \quad (10)$$

$$\left(-m_2\omega^2 + i\omega\left(c_2 + C\frac{b}{V}(\cos(\alpha_2))^2\right) + k_2\right)U_2 + i\omega\left(C\frac{b}{V}\cos(\alpha_1)\cos(\alpha_2)\right)U_1 = F_{c_2} \quad (11)$$

These equations are arranged in matrix form as shown in Eq. 12, where:

- $a_{11} = \left(-m_1\omega^2 + i\omega\left(c_1 + C\frac{b}{V}(\cos(\alpha_1))^2\right) + k_1\right)$
- $a_{12} = i\omega\left(C\frac{b}{V}\cos(\alpha_1)\cos(\alpha_2)\right)$
- $a_{21} = a_{12}$
- $a_{22} = \left(-m_2\omega^2 + i\omega\left(c_2 + C\frac{b}{V}(\cos(\alpha_2))^2\right) + k_2\right)$.

$$\begin{bmatrix} a_{11} & a_{12} \\ a_{21} & a_{22} \end{bmatrix}\begin{bmatrix} U_1 \\ U_2 \end{bmatrix} = \begin{bmatrix} F_{c_1} \\ F_{c_2} \end{bmatrix} \quad (12)$$

Using complex matrix inversion on a frequency-by-frequency basis, the direct and cross frequency response functions (FRFs) for the coupled dynamic system are obtained as shown in Eq. 13. The direct FRFs are located in the on-diagonal positions and the cross FRFs are located in the off-diagonal positions; the cross FRFs are equal because the inverted matrix is symmetric.

$$\begin{bmatrix} U_1 \\ U_2 \end{bmatrix} = \begin{bmatrix} a_{11} & a_{12} \\ a_{21} & a_{22} \end{bmatrix}^{-1}\begin{bmatrix} F_{c_1} \\ F_{c_2} \end{bmatrix} = \begin{bmatrix} \frac{U_1}{F_{c_1}} & \frac{U_1}{F_{c_2}} \\ \frac{U_2}{F_{c_1}} & \frac{U_2}{F_{c_2}} \end{bmatrix}\begin{bmatrix} F_{c_1} \\ F_{c_2} \end{bmatrix} \quad (13)$$

Tlusty [3] provided a frequency domain stability solution for regenerative chatter in turning, which defines the limiting stable chip width, b_{lim}, using Eq. 14, where $Re(G_{or})$ is the negative portion of the real part of the oriented FRF, G_{or}. This oriented FRF represents the projection of the cutting force into the mode direction and then the projection of this result in the surface normal direction.

$$b_{lim} = \frac{-1}{2K_sRe(G_{or})} \quad (14)$$

To relate the frequency-dependent b_{lim} vector to the spindle speed, Ω, Eq. 15 is applied to determine the relationship between and the valid chatter frequencies, f_c (i.e., those frequencies where $Re(G_{or})$ is negative). In this equation, N = 0, 1, 2, … is the integer number of waves per revolution (i.e., the lobe number) and $\varepsilon = 2\pi - 2\tan^{-1}\left(\frac{Re(G_{or})}{Im(G_{or})}\right)$ is the phase between the current vibration and the previous revolution.

$$\frac{f_c}{\Omega} = N + \frac{\varepsilon}{2\pi} \quad (15)$$

Tlusty's approach is extended here to develop an oriented FRF that incorporates both the direct

and cross FRFs from Eq. 13. The oriented FRF is defined using Eq. 16, where μ_{ij}, i, j = 1, 2, are the directional orientation factors:

- $\mu_{11} = \cos(\beta - \alpha_1)\cos(\alpha_1)$ projects F into u_1 to cause u_1 vibration through the direct FRF $\frac{U_1}{F_{c_1}}$ and then projects this result into y
- $\mu_{12} = \cos(\beta + \alpha_2)\cos(\alpha_1)$ projects F into u_2 to cause u_1 vibration through the cross FRF $\frac{U_1}{F_{c_2}}$ and then projects this result into y
- $\mu_{21} = \cos(\beta - \alpha_1)\cos(\alpha_2)$ projects F into u_1 to cause u_2 vibration through the cross FRF $\frac{U_2}{F_{c_1}}$ and then projects this result into y
- $\mu_{22} = \cos(\beta + \alpha_2)\cos(\alpha_2)$ projects F into u_2 to cause u_2 vibration through the direct FRF $\frac{U_2}{F_{c_2}}$ and then projects this result into y.

$$G_{or} = \mu_{11}\frac{U_1}{F_{c_1}} + \mu_{12}\frac{U_1}{F_{c_2}} + \mu_{21}\frac{U_2}{F_{c_1}} + \mu_{22}\frac{U_2}{F_{c_2}} \quad (16)$$

The direct and cross FRFs included in Eq. 16 incorporate the process damping contribution by modifying the structural damping through the terms: $i\omega\left(c_1 + C\frac{b}{V}(\cos(\alpha_1))^2\right)$, $i\omega\left(C\frac{b}{V}\cos(\alpha_1)\cos(\alpha_2)\right)$, and $i\omega\left(c_2 + C\frac{b}{V}(\cos(\alpha_2))^2\right)$ as shown in Eq. 12. The process damping contribution depends on the $\frac{b}{V}$ ratio in each case, where $V = \frac{\pi d}{60}\Omega$ (d is the workpiece diameter and Ω is expressed in rpm). Therefore, the b and Ω vectors must be known in order to modify the damping. This establishes a converging stability solution. The following steps are completed for each lobe number, N:

1. the analytical stability boundary is calculated with no process damping to identify initial b and Ω vectors
2. these vectors are used to determine the initial process damping contribution
3. the stability analysis is repeated with the new damping terms to determine updated b and Ω vectors
4. the process is repeated until the stability boundary converges.

As shown in [4-6], the solution converges rapidly (20 iterations or less is typically sufficient).

The coupled dynamics solution is now extended to two DOF in the two orthogonal directions, u_1 and u_2. From an FRF measurement in each direction, the modal parameters can be extracted (by peak picking, for example) which represent uncoupled single DOF systems in the modal coordinates q_1 and q_2 for the u_1 direction and p_1 and p_2 for the u_2 direction [7]. This modal representation requires that proportional damping holds, but this is a reasonable approximation for the lightly damped tool dynamics typically observed in practice.

Equation 5, which provides the equation of motion for the u_1 direction with a single DOF, is rewritten in Eq. 17 to describe motion in the first modal DOF, q_1. The y direction velocity is again $\dot{y} = \dot{u}_1\cos(\alpha_1) + \dot{u}_2\cos(\alpha_2)$, but $\dot{u}_1$ is now the sum of the modal velocities, $\dot{u}_1 = \dot{q}_1 + \dot{q}_2$; similarly, $\dot{u}_2 = \dot{p}_1 + \dot{p}_2$. Substitution yields Eq. 18. Equations 19-20 give the results for q_2 motion (the second modal DOF) in the u_1 direction.

$$m_{q_1}\ddot{q}_1 + c_{q_1}\dot{q}_1 + k_{q_1}q_1 = F_{c_1} - C\frac{b}{V}\dot{y}\cos(\alpha_1) \quad (17)$$

$$m_{q_1}\ddot{q}_1 + c_{q_1}\dot{q}_1 + k_{q_1}q_1 = F_{c_1} - C\frac{b}{V}\cos(\alpha_1)\left(\cos(\alpha_1)(\dot{q}_1 + \dot{q}_2) + \cos(\alpha_2)(\dot{p}_1 + \dot{p}_2)\right) \quad (18)$$

$$m_{q_2}\ddot{q}_2 + c_{q_2}\dot{q}_2 + k_{q_2}q_2 = F_{c_1} - C\frac{b}{V}\dot{y}\cos(\alpha_1) \quad (19)$$

$$m_{q_2}\ddot{q}_2 + c_{q_2}\dot{q}_2 + k_{q_2}q_2 = F_{c_1} - C\frac{b}{V}\cos(\alpha_1)\left(\cos(\alpha_1)(\dot{q}_1 + \dot{q}_2) + \cos(\alpha_2)(\dot{p}_1 + \dot{p}_2)\right) \quad (20)$$

Equations 18 and 20 are converted to the frequency domain by again assuming harmonic motion so that $q_j(t) = Q_j e^{i\omega t}$ and $p_j(t) = P_j e^{i\omega t}$, j = 1, 2. Equation 21 represents motion in Q_1 and Eq. 22 describes motion in Q_2. Even though the modal degrees of freedom are uncoupled by definition, the two equations of motion for the u_1 direction now include both Q_1 and Q_2 due to process damping. Similar to the single DOF model in the previous section, the equations also include contributions from the u_2 direction dynamics (P_1 and P_2). Interestingly, the equations of motion are coupled in both modal coordinates and the two orthogonal directions. This presents a rich dynamic system which is unlike other machining models.

$$\left(-m_{q_1}\omega^2 + i\omega\left(c_{q_1} + C\frac{b}{V}(\cos(\alpha_1))^2\right) + k_{q_1}\right)Q_1 + \left(i\omega C\frac{b}{V}(\cos(\alpha_1))^2\right)Q_2 + \left(C\frac{b}{V}\cos(\alpha_1)\cos(\alpha_2)\right)(P_1 + P_2) = F_{c_1} \quad (21)$$

$$\left(-m_{q_2}\omega^2 + i\omega\left(c_{q_2} + C\frac{b}{V}(\cos(\alpha_1))^2\right) + k_{q_2}\right)Q_2 + \left(i\omega C\frac{b}{V}(\cos(\alpha_1))^2\right)Q_1 + \left(C\frac{b}{V}\cos(\alpha_1)\cos(\alpha_2)\right)(P_1 + P_2) = F_{c_1} \quad (22)$$

Following the same approach, the frequency domain equations for the u_2 direction are presented in Eqs. 23-24, where Eq. 23 describes motion in P_1 and Eq. 24 describes motion in P_2.

$$\left(-m_{p_1}\omega^2 + i\omega\left(c_{p_1} + C\frac{b}{V}(\cos(\alpha_2))^2\right) + k_{p_1}\right)P_1 + \left(i\omega C\frac{b}{V}(\cos(\alpha_2))^2\right)P_2 + \left(C\frac{b}{V}\cos(\alpha_1)\cos(\alpha_2)\right)(Q_1 + Q_2) = F_{c_2} \quad (23)$$

$$\left(-m_{p_2}\omega^2 + i\omega\left(c_{p_2} + C\frac{b}{V}(\cos(\alpha_2))^2\right) + k_{p_2}\right)P_2 + \left(i\omega C\frac{b}{V}(\cos(\alpha_2))^2\right)P_1 + \left(C\frac{b}{V}\cos(\alpha_1)\cos(\alpha_2)\right)(Q_1 + Q_2) = F_{c_2} \quad (24)$$

Equations 21-24 are arranged in matrix form as shown in Eq. 25, where:

- $a_{11} = \left(-m_{q_1}\omega^2 + i\omega\left(c_{q_1} + C\frac{b}{V}(\cos(\alpha_1))^2\right) + k_{q_1}\right)$
- $a_{12} = i\omega\left(C\frac{b}{V}(\cos(\alpha_1))^2\right)$
- $a_{13} = i\omega\left(C\frac{b}{V}\cos(\alpha_1)\cos(\alpha_2)\right)$
- $a_{14} = i\omega\left(C\frac{b}{V}\cos(\alpha_1)\cos(\alpha_2)\right)$
- $a_{21} = a_{12}$
- $a_{22} = \left(-m_{q_2}\omega^2 + i\omega\left(c_{q_2} + C\frac{b}{V}(\cos(\alpha_1))^2\right) + k_{q_2}\right)$
- $a_{23} = i\omega\left(C\frac{b}{V}\cos(\alpha_1)\cos(\alpha_2)\right)$
- $a_{24} = i\omega\left(C\frac{b}{V}\cos(\alpha_1)\cos(\alpha_2)\right)$
- $a_{31} = a_{13}$
- $a_{32} = a_{23}$
- $a_{33} = \left(-m_{p_1}\omega^2 + i\omega\left(c_{p_1} + C\frac{b}{V}(\cos(\alpha_2))^2\right) + k_{p_1}\right)$
- $a_{34} = i\omega\left(C\frac{b}{V}\cos(\alpha_1)\cos(\alpha_2)\right)$
- $a_{41} = a_{14}$
- $a_{42} = a_{24}$
- $a_{43} = a_{34}$
- $a_{44} = \left(-m_{p_2}\omega^2 + i\omega\left(c_{p_2} + C\frac{b}{V}(\cos(\alpha_2))^2\right) + k_{p_2}\right)$.

$$\begin{bmatrix} a_{11} & a_{12} & a_{13} & a_{14} \\ a_{21} & a_{22} & a_{23} & a_{24} \\ a_{31} & a_{32} & a_{33} & a_{34} \\ a_{41} & a_{42} & a_{43} & a_{44} \end{bmatrix}\begin{bmatrix} Q_1 \\ Q_2 \\ P_1 \\ P_2 \end{bmatrix} = \begin{bmatrix} F_{c_1} \\ F_{c_1} \\ F_{c_2} \\ F_{c_2} \end{bmatrix} \quad (25)$$

Again using complex matrix inversion on a frequency-by-frequency basis, the direct and cross frequency response functions (FRFs) for the coupled dynamic system are obtained as shown in Eq. 26.

$$\begin{bmatrix} Q_1 \\ Q_2 \\ P_1 \\ P_2 \end{bmatrix} = \begin{bmatrix} a_{11} & a_{12} & a_{13} & a_{14} \\ a_{21} & a_{22} & a_{23} & a_{24} \\ a_{31} & a_{32} & a_{33} & a_{34} \\ a_{41} & a_{42} & a_{43} & a_{44} \end{bmatrix}^{-1}\begin{bmatrix} F_{c_1} \\ F_{c_1} \\ F_{c_2} \\ F_{c_2} \end{bmatrix} = \begin{bmatrix} \frac{Q_{1,1}}{F_{c_1}} & \frac{Q_{1,2}}{F_{c_1}} & \frac{Q_{1,3}}{F_{c_2}} & \frac{Q_{1,4}}{F_{c_2}} \\ \frac{Q_{2,1}}{F_{c_1}} & \frac{Q_{2,2}}{F_{c_1}} & \frac{Q_{2,3}}{F_{c_2}} & \frac{Q_{2,4}}{F_{c_2}} \\ \frac{P_{1,1}}{F_{c_1}} & \frac{P_{1,2}}{F_{c_1}} & \frac{P_{1,3}}{F_{c_2}} & \frac{P_{1,4}}{F_{c_2}} \\ \frac{P_{2,1}}{F_{c_1}} & \frac{P_{2,2}}{F_{c_1}} & \frac{P_{2,3}}{F_{c_2}} & \frac{P_{2,4}}{F_{c_2}} \end{bmatrix}\begin{bmatrix} F_{c_1} \\ F_{c_1} \\ F_{c_2} \\ F_{c_2} \end{bmatrix} \quad (26)$$

The direct FRFs in the u_1 and u_2 directions are defined by Eqs. 27-28, respectively; the cross FRFs are provided in Eqs. 29-30. The oriented FRF is again calculated using Eq. 16 and the directional orientation factors are the same.

$$\frac{U_1}{F_{c_1}} = \frac{Q_{1,1}}{F_{c_1}} + \frac{Q_{1,2}}{F_{c_1}} + \frac{Q_{2,1}}{F_{c_1}} + \frac{Q_{2,2}}{F_{c_1}} \quad (27)$$

$$\frac{U_2}{F_{c_2}} = \frac{P_{1,3}}{F_{c_2}} + \frac{P_{1,4}}{F_{c_2}} + \frac{P_{2,3}}{F_{c_2}} + \frac{P_{2,4}}{F_{c_2}} \quad (28)$$

$$\frac{U_2}{F_{c_1}} = \frac{P_{1,1}}{F_{c_1}} + \frac{P_{1,2}}{F_{c_1}} + \frac{P_{2,1}}{F_{c_1}} + \frac{P_{2,2}}{F_{c_1}} \quad (29)$$

$$\frac{U_1}{F_{c_2}} = \frac{Q_{1,3}}{F_{c_2}} + \frac{Q_{1,4}}{F_{c_2}} + \frac{Q_{2,3}}{F_{c_2}} + \frac{Q_{2,4}}{F_{c_2}} \quad (30)$$

The model may be extended to additional DOFs in each direction. For three DOFs in each direction, for example, Eq. 25 becomes a 6×6 symmetric matrix. The direct and cross FRFs are then a sum of six, rather than four, terms from the inverted matrix.

To demonstrate the multiple DOF algorithm, consider the model in Fig. 1 with α_1 = 30 deg, α_2 = 60 deg, β = 70 deg, K_s = 2000 N/mm^2, C = 200 N/mm, and d = 75 mm for an outer diameter turning operation. The structural dynamics are symmetric with a modal stiffness of 7×10^6 N/m, a natural frequency of 600 Hz, and a viscous modal

damping ratio of 0.03 (3%) for the first mode and a modal stiffness of 9×10^6 N/m, a natural frequency of 900 Hz, and a viscous modal damping ratio of 0.03 (3%) for the second mode. The corresponding stability limit with process damping effects is displayed in Fig. 2. To validate the predicted stability limit, the modal equations of motion were solved by Euler (numerical) integration in a time domain simulation [7]. Stable {spindle speed, chip width} combinations are identified by circles and unstable combinations are represented by squares in Fig. 2. Good agreement is observed.

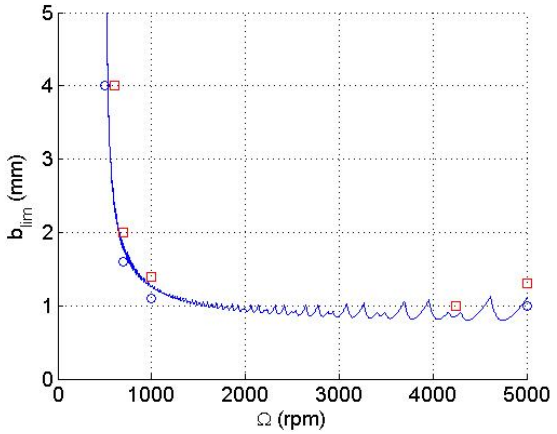

Figure 2: Comparison of analytical stability limit and time domain simulation results for turning model with 2DOF in two orthogonal directions. Stable {spindle speed, chip width} combinations are identified by circles and unstable combinations are represented by squares.

RESULTS

Low-speed cutting tests were performed in order to validate the multiple degree of freedom process damping model and calculate a process damping coefficient. The experiments were carried out on a Haas TL-1 CNC lathe. A custom notch hinge flexible cutting tool was designed to provide a multiple degree of freedom (DOF) system in the feed direction of the cutting operation; see Figure 3.

A tube turning geometry was selected for the cutting tests. In this arrangement, the feed direction is parallel to the tube axis. Because the flexure compliance was much higher than the workpiece in the feed direction, the stability analysis was completed using the flexure's dynamic properties only. The frequency response function and modal parameters for the flexure in the feed and tangential directions are provided in Table 1.

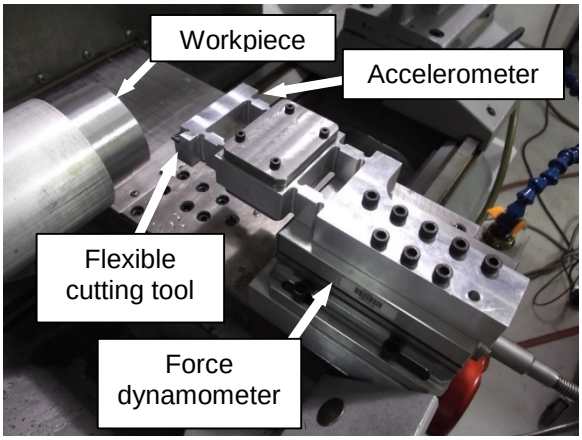

Figure 3: Experimental setup for turning stability tests. A cutting force dynamometer and accelerometer (not shown) were used to monitor the cutting process.

Table 1: Modal parameters for flexible cutting tool setup.

Direction	Viscous damping ratio (%)	Modal stiffness ($\times10^7$ N/m)	Natur. freq. (Hz)
Tangential	7.21	3.71	703
Feed	6.23	0.80	303
	9.01	0.96	405
	1.68	1.88	1433

The workpiece material for all cutting tests was 6061-T6 aluminum. The wall thickness of the tube was varied, while a constant mean workpiece diameter of 87 mm was maintained for all experiments. The cutting insert (Kennametal SPEB322) was TiN coated with an 11 deg relief angle, 0 deg rake angle, and no chip breaker. The commanded chip width, b, varied between 1.0 mm and 3.0 mm and the cutting speed range was 82-273 m/min (300-1000 rpm). The feed rate was held constant at 0.13 mm/rev.

Before stability testing was completed, the force model for the workpiece/cutter combination was identified. This was achieved under stable cutting conditions using an off-the-shelf lathe insert holder that held the same insert as the manufactured flexible tool. The inserted holder was mounted to the cutting force dynamometer. The force model was calculated at both 500 and 1000 rpm for b = 1 mm and feed rate of 0.13 mm/rev. The mean values were K_s = 1343±32 N/mm^2 (which scales the chip area to obtain the resultant cutting force) and β = 55° (the force angle).

The stability was identified using an accelerometer (PCB Piezotronics model 352B10) and cutting force dynamometer (Kistler model 9257B). The force and vibration levels, as well as the frequency content of the two signals, were used to establish stable/unstable performance. Also, qualitatively, the machined surface finish after each test cut was inspected using a digital microscope.

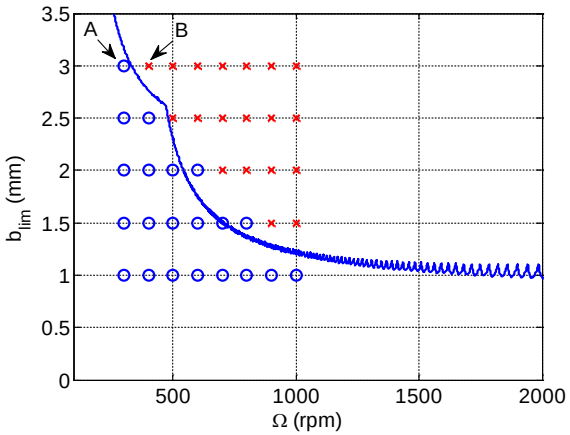

Figure 4: Stability boundary for the multi-degree of freedom system with the grid of stable (o) and unstable (x) cutting tests (C = 1.3×10^5 N/m).

A grid of low-speed test points was selected to investigate the process damping behavior for the multi-degree of freedom system; see Figure 4. A process damping coefficient, C, was estimated based on a single variable residual sum of squares (RSS) minimization that best represented the stability boundary [6]. A process damping coefficient value of C = 1.3×10^5 N/m was found to best represent the stability boundary. This results agrees with previously reported data for a SDOF setup [6].

CONCLUSIONS

An analytical stability model was presented which accounts for multiple degree of freedom vibratory systems in turning applications. The model includes a process damping force in the surface normal direction which depends on the depth of cut, the cutting speed, the tool velocity, and an empirical process damping coefficient.

REFERENCES

[1] P.W. Wallace, C. Andrew, Machining forces: Some effects of tool vibration, Journal of Mechanical Engineering Science, 7 (1965) 152-162.

[2] Y. Altintas, M. Eynian, H. Onozuka, Identification of dynamic cutting force coefficients and chatter stability with process damping, Annals of the CIRP, 57/1 (2008) 371-374.

[3] J. Tlusty, M. Polacek, The stability of machine tools against self-excited vibrations in machining, in: Proceedings of the ASME International Research in Production Engineering Conference, Pittsburgh, PA, 1963, pp. 465-474.

[4] C. Tyler, T. Schmitz, Process damping analytical stability analysis and validation, Transactions of the NAMRI/SME, 40 (2012).

[5] C. Tyler, J. Karandikar, T. Schmitz, T., Process damping coefficient identification using Bayesian inference, Transactions of the NAMRI/SME, 41 (2013).

[6] C. Tyler, T. Schmitz, Analytical process damping stability prediction, Journal of Manufacturing Processes, 15 (2013) 69-76.

[7] T. Schmitz, S. Smith, Machining Dynamics: Frequency Response to Improved Productivity, Springer, New York, NY, 2009.